7-1-2016

Characterizing active and inactive brown adipose tissue in adult humans using PET-CT and MR imaging

Aliya Gifford
Vanderbilt University

Theodore F. Towse
Grand Valley State University, towset@gvsu.edu

Ronald C. Walker
Vanderbilt University

Malcolm J. Avison
Vanderbilt University

E Brian Welch
Vanderbilt University

Characterizing active and inactive brown adipose tissue in adult humans using PET-CT and MR imaging

Aliya Gifford,[1,2] Theodore F. Towse,[1,3] Ronald C. Walker,[4,5] Malcolm J. Avison,[1,2,5,6] and E. Brian Welch[1,2,5]

[1]*Vanderbilt University Institute of Imaging Science, Nashville, Tennessee;* [2]*Chemical and Physical Biology Program, Vanderbilt University, Nashville, Tennessee;* [3]*Department of Physical Medicine and Rehabilitation, Vanderbilt University School of Medicine, Nashville, Tennessee;* [4]*Department of Medical Imaging, Tennessee Valley Veterans Affairs Healthcare, Nashville, Nashville, Tennessee;* [5]*Department of Radiology and Radiological Sciences, Vanderbilt University School of Medicine, Nashville, Tennessee; and* [6]*Department of Pharmacology, Vanderbilt University School of Medicine, Nashville, Tennessee*

Gifford A, Towse TF, Walker RC, Avison MJ, Welch EB. Characterizing active and inactive brown adipose tissue in adult humans using PET-CT and MR imaging. *Am J Physiol Endocrinol Metab* 311: E95–E104, 2016. First published May 10, 2016; doi:10.1152/ajpendo.00482.2015.—Activated brown adipose tissue (BAT) plays an important role in thermogenesis and whole body metabolism in mammals. Positron emission tomography (PET)-computed tomography (CT) imaging has identified depots of BAT in adult humans, igniting scientific interest. The purpose of this study is to characterize both active and inactive supraclavicular BAT in adults and compare the values to those of subcutaneous white adipose tissue (WAT). We obtained [^{18}F]fluorodeoxyglucose ([^{18}F]FDG) PET-CT and magnetic resonance imaging (MRI) scans of 25 healthy adults. Unlike [^{18}F]FDG PET, which can detect only active BAT, MRI is capable of detecting both active and inactive BAT. The MRI-derived fat signal fraction (FSF) of active BAT was significantly lower than that of inactive BAT (means ± SD; 60.2 ± 7.6 vs. 62.4 ± 6.8%, respectively). This change in tissue morphology was also reflected as a significant increase in Hounsfield units (HU; −69.4 ± 11.5 vs. −74.5 ± 9.7 HU, respectively). Additionally, the CT HU, MRI FSF, and MRI R_2^* values are significantly different between BAT and WAT, regardless of the activation status of BAT. To the best of our knowledge, this is the first study to quantify PET-CT and MRI FSF measurements and utilize a semiautomated algorithm to identify inactive and active BAT in the same adult subjects. Our findings support the use of these metrics to characterize and distinguish between BAT and WAT and lay the foundation for future MRI analysis with the hope that some day MRI-based delineation of BAT can stand on its own.

tissue segmentation; fat water magnetic resonance imaging; fat signal fraction; brown adipose tissue; white adipose tissue

IT HAS BEEN KNOWN FOR SOME TIME that the primary role of brown adipose tissue (BAT) is to generate heat in response to cold (10, 32, 55). More recent evidence shows BAT also performs as an endocrine organ, secreting adipokines that signal multiple tissues (39, 48) and organs (60). BAT also plays a role in whole body metabolism, assisting with glucose homeostasis and insulin sensitivity (13, 40). For example, a model of diabetic mice received BAT transplants, resulting in an insulin-independent reversal of type 1 diabetes (22). Additionally, active

BAT in mice can clear 75% of the glucose and 50% of the triglycerides from circulation (5). Much of our understanding of BAT comes from animal models. However, the rediscovery of BAT in adult humans has ignited tremendous scientific interest.

Studies show evidence that cold-activated BAT is present in adults (54, 56a, 58). There is some indication that the presence of BAT in humans is dependent on ethnicity (4), declines with age (24, 50), and is inversely correlated with obesity (57). Some smaller ($n < 6$) studies report a prevalence of BAT in adults as high as 100% (15, 59); however, larger studies report a range of 20–96% (56a, 57). Our understanding of human BAT is somewhat limited because the primary technique for detecting BAT is through [^{18}F]fluorodeoxyglucose ([^{18}F]FDG) positron emission tomography (PET) imaging. Although [^{18}F]FDG PET is useful for detecting glucose metabolism of tissues, it is important to note that active BAT of mice and humans preferentially combusts fatty acids (4–6, 49). These fatty acids are derived from plasma triglycerides after lipolysis, which is fueled by glucose (6, 35). Therefore, [^{18}F]FDG PET does not always detect metabolically active BAT, but the observation of increased levels of [^{18}F]FDG uptake are a reliable indication of activated BAT. That is to say, [^{18}F]FDG is highly specific but not highly sensitive to activated BAT. In this work, the term "active BAT" is used to indicate BAT that exhibits increased levels of [^{18}F]FDG, although it is possible for active BAT to exist without taking up [^{18}F]FDG. An additional limitation of PET imaging is due to its use of ionizing radiation. Therefore, to fully understand the function of BAT and its role in whole body energy metabolism, new imaging techniques need to be employed.

Magnetic resonance imaging (MRI) has already been proposed as an alternative BAT imaging technique (37). MRI is useful partly because it does not use ionizing radiation, and therefore, longitudinal studies are possible. Additionally, unlike PET, MRI can detect BAT under thermoneutral (nonactivated) conditions and has been used to measure BAT volume and activity (11, 52, 56b). Using MRI to detect the differences between BAT and white adipose tissue (WAT) is possible because BAT and WAT have unique characteristics. White adipocytes contain a single large lipid vacuole and few mitochondria (2). Brown adipocytes contain multiple lipid vacuoles and an abundance of iron-rich mitochondria (10). Therefore, fat occupies a higher fraction of total cell volume in WAT than in BAT, which can be measured using the MRI property called

Address for reprint requests and other correspondence: E. B. Welch, Vanderbilt University Institute of Imaging Science, 1161 21st Ave. South, Medical Center North, AA-1105, Nashville, TN 37232-2310 (e-mail: brian.welch@vanderbilt.edu).

fat signal fraction (FSF). In mice, gonadal WAT has a FSF of 90–93%, and interscapular BAT ranged from 40 to 80% FSF. Humans aged 5–26 yr also show a FSF of 39.2–80.6% in clavicular BAT and 87.4–96.0% FSF in subcutaneous WAT (30). Additionally, BAT has higher iron content due to the elevated mitochondrial density and blood vessel innervation in BAT compared with WAT. The MR property called transverse signal decay rate (R_2^*), which is related to T_2^* relaxation time as $R_2^* = 1/T_2^*$, may reflect the tissue iron content (1, 34, 62). In infants and adolescents, R_2^* of supraclavicular BAT ranges from 39 to 84 s^{-1}, and subcutaneous WAT ranges from 22 to 40 s^{-1} (30, 31).

The purpose of this research was to quantify the PET-CT and MRI characteristics of active and inactive clavicular BAT in healthy adult subjects and to compare these with the values in subcutaneous WAT. Additionally, this work aims to determine whether MRI is capable of detecting a difference between active and inactive BAT. This would prove useful, as [18F]FDG PET can only detect activated BAT. Finally, this work quantifies image-based adipose tissue metrics in both PET-positive and PET-negative subjects. In this work, the term "PET positive" indicates subjects whose clavicular BAT had increased [18F]FDG levels after exposure to cold, and "PET negative" indicates subjects who did not.

To delineate regions of clavicular BAT, this work makes use of our previously reported automated segmentation technique (16). This segmentation method produces a conservative estimate of clavicular BAT and minimizes the effect of rater subjectivity and boundary ambiguity on the results. The rigorously defined MRI properties of BAT presented in this work lay the foundation for MRI-based quantitative imaging of BAT without the need for the ionizing radiation and the radioactive tracers required to obtain PET-CT images.

MATERIALS AND METHODS

Subject and study setup. The local ethics committee of Vanderbilt University approved this study, and all subjects provided written, informed consent prior to participation. Twenty-five healthy adults participated in the study. To be eligible for the study, subjects had to be between the ages of 18 and 45 yr and with a body mass index (BMI) between 18.5 and 30 kg/m². Additionally, the subjects were screened for the following exclusion criteria: diabetes mellitus, use of β-blockers or anxiety medication, history of smoking or chewing tobacco products, and consumption of more than four cups of coffee each day or more than two alcoholic drinks each day.

Four imaging scan sessions were acquired on all subjects: two MRI and two PET-CT, with each scan session acquired on a different day and all four scans completed on average within a 5-wk timespan. Both scanning modalities were performed under thermoneutral 24°C (75.2°F) and cold 17°C (62.6°F) conditions. All scans were performed in the morning, with each study day completed by 1300. Subjects were required to refrain from alcohol, caffeine, medication, and exercise or strenuous activity for 24 h prior and to fast overnight (≥8 h). The full details of the temperature-controlled room and subject setup were described previously (21) but are briefly summarized here. The room temperature was maintained without air blowing directly on the subject. Prior to entering the temperature-controlled room, subjects changed into standardized disposable hospital exam shorts and t-shirts (MediChoice, Mechanicsville, VA). Subjects also removed socks and shoes, keeping their underwear on, resulting in a total clo factor (8) of 0.19 clo (female: underwear 0.03 clo, bra 0.01 clo, shorts 0.06 clo, t-shirt 0.09 clo; male: briefs 0.04 clo, shorts 0.06

clo, t-shirt 0.09 clo). Subjects' height, weight, and waist circumference measurements were taken after changing into standard clothing.

Subjects then sat stationary for 2 h in the temperature-controlled room before being scanned. They were allowed to read or watch television but were not allowed to perform any activity that could change their body temperature, i.e., exercise or sleep. After these 2 h, the subjects were transported to either the MRI or PET-CT scanner by wheelchair to minimize potential warming due to muscular activity. Additionally, body temperature measurements were made on four occasions using a sublingual thermometer: prior to entering the temperature-controlled room, after 1 h in the room, at the end of the 2 h, and finally within 5 min after scan completion.

Image acquisition. PET-CT scans were acquired on a GE Discovery See and Treat Elite (STE) PET-CT scanner (General Electric Medical Systems, Milwaukee, WI) with a field of view covering from the crown of the head to midthigh using seven to nine bed positions, depending on subject height (2 min/bed position). Scans were acquired in helical mode with a 0.8-s revolution time, a 1.25-mm single collimation width, and a 1.675 spiral pitch factor. The reconstructed PET-CT voxel sizes are as follows: PET, 5.5 mm × 5.5 mm in-plane, and 3.27 mm through-plane; CT, 1.37 mm × 1.37 mm in-plane and 3.27 mm through-plane. For PET-CT scans, a nuclear medicine technologist administered the injection of [18F]FDG intravenously after the first hours in the temperature-controlled room. The total [18F]FDG dosage was calculated based on subject weight at 0.14 mCi/kg.

MRI scans were acquired using a Philips Achieva 3T (Philips Healthcare, Best, The Netherlands) scanner equipped with two-channel parallel transmit capability, a 16-channel Torso-XL surface coil (Invivo, Gainesville, FL), and an X-tend tabletop (X-tend ApS, Hornslet, Denmark). The modified MRI table setup has been described previously (21). The MRI sequence was a multi-stack, multi-slice, multiple fast field echo (FFE) acquisition with 12 stacks of 20 contiguous axial slices. Scanner software was modified to enable the sampling of eight echoes acquired as two interleaved sets of four echoes, with first echo time being $TE_1 = 1.024$ ms and effective echo time spacing $\Delta TE = 0.779$ ms. Preparation phases for each stack included center frequency (F_0) optimization and first order linear B_0 shimming. Additional acquisition details include flip angle = 12°, repetition time (TR) = 83 ms, water fat shift = 0.323 pixels, readout sampling bandwidth = 1,346.1 Hz/pixel, axial in-plane field of view = 520 mm × 408 mm, acquired voxel size = 2 mm × 2 mm × 7.5 mm, and sensitivity encoding (SENSE) parallel imaging factor = 3 in the anterior-posterior direction. Acquisition time was 25 s/stack, and two breath holds were performed per station from the neck to the pelvis. Real and imaginary images were saved for off-line processing.

Additional MRI scans acquired prior to each stack included a dual-angle B_1 calibration scan (acquisition time 15.1 s) that was acquired to enable optimized RF shimming for the two-channel transmit capability of the scanner and a SENSE reference scan (acquisition time 12.1 s).

Image processing. The MRI reconstruction and water-fat image separation steps were performed using a robust hybrid magnitude- and complex-based method (65). Prior to analysis, the first echo of each four-echo train was discarded to avoid potential phase contamination by eddy currents in the complex water-fat signal (26). Then the complex three-dimensional water-fat separation and R_2^* estimation was performed based on a multiscale whole image optimization algorithm (7). Fat was modelled using a six-peak spectral model that was validated previously for multiple anatomies and scanner field strengths (47, 56, 61). In addition to better modeling of fat, a multipeak fat spectrum model was used because, in the presence of fat, multipeak fat modeling is necessary for improved R_2^* mapping (25). The resulting magnitude images of water, fat, and R_2^* were then used to fit the magnitude of all sampled data to achieve a robust hybrid magnitude- and complex-based method (65) and generate final water

and fat images. These final water and fat magnitude images were then used to calculate a fat-signal fraction (FSF) image using

$$FSF = \frac{fat}{water + fat}$$

in voxels where the signal was greater in the fat image (fat dominant) and

$$FSF = 1 - \frac{water}{water + fat}$$

in voxels where signal was greater in the water image (water dominant). For the explanation of converting CT data to images in Hounsfield units (HU) and the PET data to images in standardized uptake values (SUV), see our previously published work (21).

To enable analysis of the same anatomic region of interest of a subject in each of the four scans, all image volumes were coregistered for each subject individually. Registration was performed using a semiautomated method with in-house developed 3-plane-view software using a rigid body registration algorithm (45). Due to difficulties with registering the entire image volume across all four scans, emphasis was placed on registering the region covering the chin to heart. During registration, the MRI and PET data underwent partial volume interpolation, resulting in the same voxel dimensions as the CT data. It should be noted that although interpolation of the data could introduce errors, it was a required step in the registration method used. However, steps such as boundary erosion were taken to reduce the partial volume effects, as described below.

Following image registration, a subject-specific binary mask of the clavicular BAT depot in PET-positive subjects was created using our previously published method (21). The large range of HU values used in this method was implemented to not artificially limit the range of possible HU values, as it was unknown what type of adipose tissue existed in the clavicular depot of these subjects. The mask was limited for each subject to include only slices that covered from the C3 vertebrae to the aortic arch. The cropped BAT mask was then applied to allof the coregistered images to evaluate the HU, SUV, FSF, and R_2* values in the BAT depots for both the thermoneutral and cold scan. Use of this automated method minimized the effect of rater subjectivity and boundary ambiguity, thus enabling objective analysis of the same region of tissue in all coregistered images for a given subject.

For comparison with clavicular BAT, umbilicus level subcutaneous WAT was segmented in the same subjects. Prior to the WAT depot being segmented, the images for each subject were first registered again, with the focus instead on the lower abdomen. To be included in the mask, a voxel had to fulfill all of the following requirements: *1*) CT HU values between −200 and −1 HU (36, 64), *2*) MRI FSF values between 85 and 100% fat (29, 30), and *3*) MRI R_2* values <200 s^{-1} (29).

Any visceral adipose tissue included in this mask was removed manually, using both the MRI and CT images as guides. The boundary of the resulting subcutaneous WAT mask was eroded to reduce any partial volume effects, and 10 slices at the umbilicus level were selected for each subject.

To analyze the clavicular adipose tissue of PET-negative subjects, a mask was created from their coregistered images using the following rules: *1*) CT HU values between −200 and −1 HU, *2*) MRI FSF range from 50 to 100% fat, *3*) MRI R_2* <150 s^{-1}, and *4*) no limits on SUV.

The resulting mask was limited to the clavicular adipose region, manually excluding any subcutaneous WAT from the mask using both the CT HU and MRI FSF images as visual guides. The umbilicus level subcutaneous WAT masks for the PET-negative subjects were created using the same rules listed above.

Data analysis. Except where noted, image analysis was performed using in-house-developed MATLAB 2014a (Mathworks, Natick, MA) scripts, and statistical analysis was performed in RStudio version

0.98.1091 (RStudio, Boston, MA). Analysis was first conducted on all 17 subjects as one group. Following this, the subjects were divided into two groups based on BMI, normal weight (BMI <25.0) and overweight (BMI ≥25.0), to perform an ad hoc analysis to explore any potential differences present. Prior to comparing thermoneutral and cold data for the whole group, the data were first tested for normality to determine whether a parametric or nonparametric statistical test should be used. Testing for normality was performed using three methods. First, a histogram of the data was plotted and visually inspected to determine whether the histogram appeared to be normally distributed; second, a quantile-quantile plot of the data was visually inspected for linearity, and third, the Shapiro-Wilk test was used to test for normality, given the null hypothesis that the data are normal and a *P* value >0.05 indicating that the null hypothesis cannot be rejected. When comparing thermoneutral and cold data for the normal weight and overweight BMI groups, nonparametric tests are used because it is not meaningful to test for normality in groups with small numbers. Data are presented as means ± SD, unless otherwise noted.

RESULTS

Of the 25 subjects enrolled, 20 subjects showed increased [18F]FDG uptake in the clavicular adipose tissue; 19 subjects showed increased uptake after exposure to cold and low uptake after thermoneutral exposure, and one subject showed increased uptake after thermoneutral exposure and low uptake after exposure to cold. In this work, we refer to these 19 subjects as PET positive for BAT, corresponding with previously published findings. From these 19 subjects, only 17 are included in this study (6 male): age 25.1 ± 2.9 yr and body mass index (BMI) 23.9 ± 2.9 kg/m^2 (Table 1). A complete flow chart explaining the breakdown of all 25 subjects is given in Fig. 1.

Analysis of the PET-positive subject characteristics revealed that neither age nor height was different between the normal and overweight groups. This removes both age and height as confounding factors when determining which characteristics

Table 1. *Subject characteristics*

Characteristic	Normal BMI <25.0 (*n* = 12)	Overweight BMI ≥25 (*n* = 5)
n (Male)	12 (4)	5 (2)
Age, yr		
Mean	24.5 ± 1.8	26.5 ± 4.1
Range	21.6–27.9	23.1–34.5
Height, cm		
Mean	167.7 ± 6.2	166.1 ± 8.9
Range	157.0–176.5	153.5–176.5
Weight, kg		
Mean	63.2 ± 6.6	75.9 ± 8.4*
Range	52.4–74.7	64.9–85.9
BMI, kg/m^2		
Mean	22.4 ± 1.4	27.5 ± 2.1**
Range	20.2–24.7	25.3–31.5
Waist, cm		
Mean	73.8 ± 2.3	82.0 ± 6.6*
Range	69.0–78.8	73.0–89.3

Values are means ± SD. BMI, body-mass index; waist, waist circumference measured at umbilicus. This shows that the age and height are not different between the normal and overweight subjects. Therefore, age is not a confounding factor in considering which properties may affect brown adipose tissue characteristics between subjects. However, the population distribution of weight, BMI, and waist circumference are right-shifted (larger valued) in overweight subjects compared with normal-weight subjects. *P <0.05; **P <0.001, using the Mann-Whitney *U*-test to compare normal with overweight subjects.
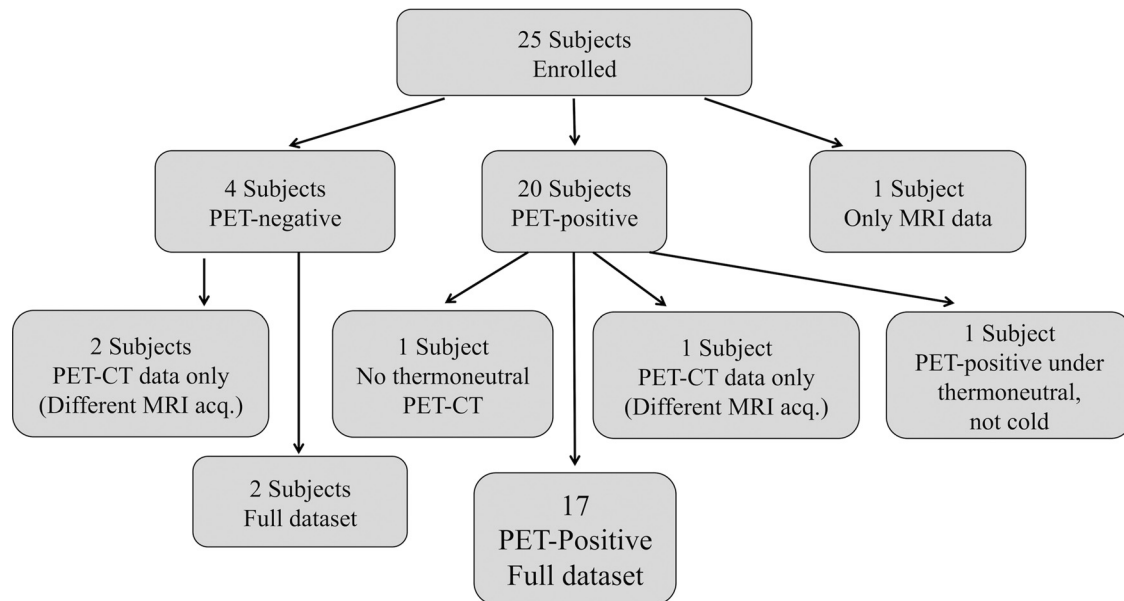
Fig. 1. Flow chart showing complete subject recruitment and data acquisition. PET-CT, positron emission tomography-computed tomography.

may affect the differences in BAT between these two groups. However, weight, BMI, and waist circumference were significantly higher in the overweight subjects (Table 1). Other potential contributors to visualizing BAT activation were also analyzed for differences between the subjects. These potential contributors were fasting glucose level, body temperature, and outdoor temperature (33, 50). Fasting blood glucose levels were not significantly different between the thermoneutral and cold PET-CT scans for all 17 subjects [89.6 ± 6.1 (thermoneutral) and 86.5 ± 8.4 mg/dl (cold), $P = 0.52$] or for the normal-weight [90.8 ± 5.4 (thermoneutral) and 85.8 ± 7.5 mg/dl (cold), P value = 0.19] and overweight [85.8 ± 7.1 (thermoneutral) and 88.4 ± 11.1 mg/dl (cold), $P = 0.27$] groups. However, the subjects' body temperature after 2 h in the temperature-controlled room ($\Delta T = T_{hour\ 2} - T_{hour\ 0}$) increased significantly in the thermoneutral room (means ± SD; $\Delta T = 0.29 \pm 0.68°F$, $P = 0.02$) and decreased significantly in the cold room ($\Delta T = -0.15 \pm 0.53°F$, $P = 0.02$). Outdoor temperature was not significantly different for the week prior to thermoneutral scans vs. the week prior to cold scans (thermoneutral scan week: 34.6 ± 16.0°F vs. cold scan week: 34.4 ± 15.5°F, $P = 0.9$).

Coronal PET-CT and MRI images from a representative normal-weight and overweight subject are shown in Fig. 2 and Fig. 3, respectively. The normal-weight subject shows areas of increased SUV on the cold PET maximum intensity projection (MIP) image (Fig. 2E, red arrows) compared with the warm PET MIP (Fig. 2A). Although not as intense as the normal-weight subject, the overweight subject also shows increased SUV on the cold PET MIP (Fig. 3E, red arrows). The regions also appear smaller with no accompanying paraspinal depots, which are visible on the normal-weight subject. Single coronal slices of CT HU (Figs. 2, B and F, and 3, B and F), PET SUV (Figs. 2, C and G, and 3 C and G), and MRI FSF (Figs. 2, D and H, and 3, D and H) are also displayed. The clavicular regions of elevated SUV during the cold scan (Figs. 2G and 3G) correspond to regions with the radio density of adipose

tissue on the CT images (Figs. 2, B and F, and 3, B and F). The same region of adipose tissue is clearly visible on the corresponding MRI FSF images [Figs. 2, D (white ovals) and H, and 3, D (white ovals) and H], with FSF values in the range of 50–70% fat. Unlike the uptake of [^{18}F]FDG in the PET images, this region of tissue is visible under both thermoneutral and cold conditions. Axial slices from the cold scan of the subjects depicted in Figs. 2 and 3 can be seen in Fig. 4.

The thermoneutral and cold MRI FSF and R_2^*, CT HU, and PET SUV values of clavicular BAT from the 17 PET-positive subjects are plotted in Fig. 5. The data are plotted keeping all subjects as a group as well as for the normal-weight and overweight groups. These results show that the FSF, HU, and SUV values are distinct between the thermoneutral and cold scans for the whole group. Specifically, the FSF of clavicular BAT is higher in the thermoneutral compared with the cold scan for all subjects: thermoneutral, 62.4 ± 6.8%; cold, 60.2 ± 7.6% ($P < 0.05$). The mean FSF for normal-weight subjects was 61.0 ± 5.9 vs. 65.7 ± 8.5% for the overweight subjects in the thermoneutral condition and 59.2 ± 7.0% vs. 62.6 ± 9.4% for the normal vs. overweight subjects in the cold condition. The mean HU of clavicular BAT for normal-weight vs. the overweight subjects were as follows: thermoneutral −71.2 ± 10.6 HU vs. −76.7 ± 4.7 HU and cold −66.6 ± 10.9 HU vs. −71.5 ± 14.4 HU, respectively. As expected, the mean clavicular BAT SUV was significantly higher in all subjects after exposure to cold (5.0 ± 2.0 g/ml) compared with the thermoneutral condition (0.6 ± 0.5 g/ml, $P < 1e^{-5}$). The SUV was not significantly greater in normal-weight subjects (5.4 ± 2.1 g/ml) compared with overweight subjects (4.1 ± 1.4 g/ml) after cold exposure ($P = 0.16$).

The clavicular BAT values from the 17 PET-positive subjects are plotted compared with their subcutaneous WAT values for both the thermoneutral and cold scans in Fig. 6. The HU, FSF, and R_2^* values are all significantly different between the two adipose tissues; the HU values are significantly higher (less negative), the FSF values are significantly lower, and the
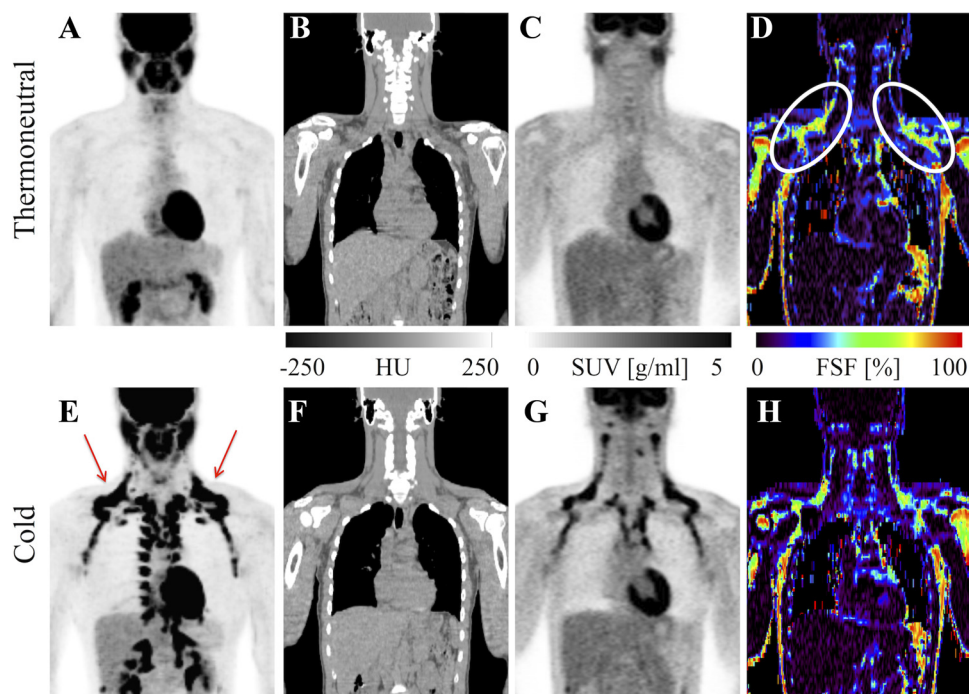
Fig. 2. Example images from the thermoneutral (*A–D*) and cold (*E–H*) scans of a subject from the normal-weight group: male, 22 yr old, body mass index (BMI) = 20.2 kg/m². Uptake of [¹⁸F]fluorodeoxyglucose ([¹⁸F]FDG) characteristic of brown adipose tissue is visible in the clavicular area in the cold PET maximum intensity projection (MIP; *E*, red arrows) and is distinctly absent from the thermoneutral PET MIP (*A*). Coronal CT slice shows the region of clavicular tissue with adipose Hounsfield units (HU) in both the thermoneutral and cold scans (*B* and *F*). The corresponding coronal PET slices (*C* and *G*) show the increased standardized uptake value (SUV) in the clavicular adipose tissue after exposure to cold. Corresponding coronal slices of the MRI-derived fat signal fraction (FSF, %) maps (*D* and *H*) show clavicular depots with a FSF in the range of 50–70% (white ovals). The anatomic location corresponds to the clavicular regions with high SUV on the cold PET scan, and the FSF range agrees with previously published values of brown adipose tissue (BAT) (30, 31). Unlike in the PET scan, this region of tissue is visible on MRI regardless of temperature.

R_2^* values are significantly higher in BAT than in WAT. Additionally, the range of FSF values in BAT is much greater than WAT in both the thermoneutral and cold scans. For example, thermoneutral BAT ranges from 51.6 to 78.7% FSF, whereas thermoneutral WAT ranges from 89.0 to 95.1% FSF.

Also plotted in Fig. 6 are the values of the supraclavicular adipose tissue and subcutaneous WAT from the PET-negative subjects. Their results are plotted next to the BAT and WAT of all 17 PET-positive subjects for comparison. Interestingly, the PET-negative subjects' HU values of both the supraclavicular

adipose tissue and subcutaneous WAT are spread across the full range of values seen in the PET-positive subjects (Fig. 6*A*). However, both the FSF and R_2^* values of the two tissue regions are more tightly clustered and distinguishable for the PET-negative subjects (Fig. 6, *B* and *C*). The FSF values of the PET-negative supraclavicular adipose tissue are in the upper quartile of the PET-positive BAT values, indicating a trend toward the WAT values. The R_2^* values also reflect this trend, where the PET-negative supraclavicular adipose tissue R_2^* values occupy the lower quartile of the PET-positive BAT
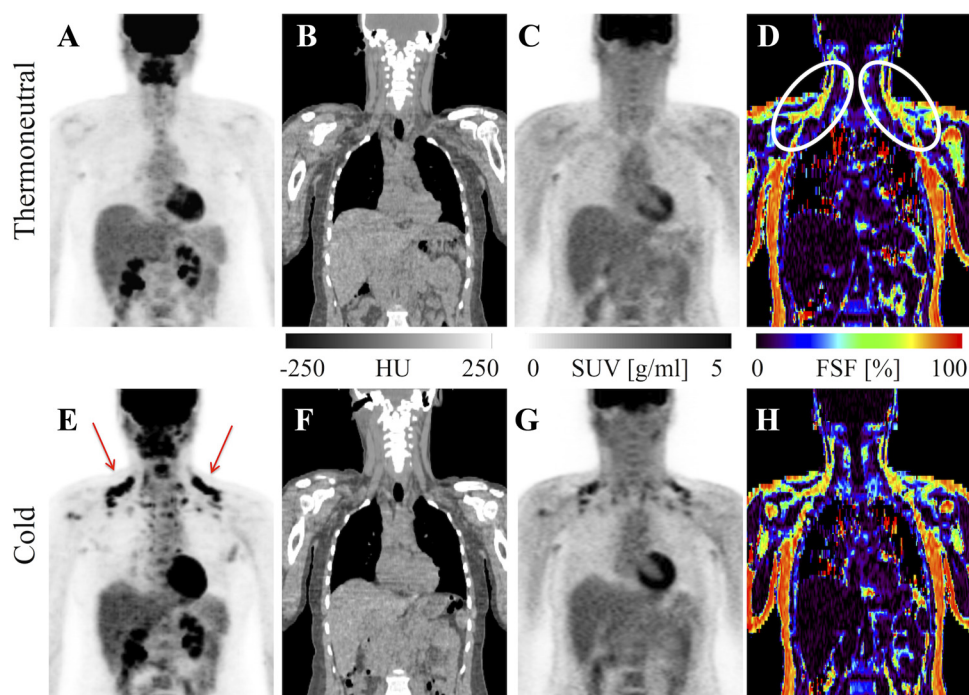

Fig. 3. Example images from the thermoneutral (*A–D*) and cold (*E–H*) scans of a subject from the overweight group: female, 34 yr old, BMI = 27.5 kg/m². Characteristic uptake of [¹⁸F]FDG in brown adipose tissue is visible in the clavicular area in the cold PET maximum intensity projection (MIP; *E*, red arrows) and is distinctly absent from the thermoneutral PET MIP (*A*). Coronal CT slices show the region of clavicular tissue with adipose Hounsfield units (HU) in both the thermoneutral and cold scans (*B* and *F*). The corresponding coronal PET slices (*C* and *G*) show the increased standardized uptake value (SUV) in the clavicular adipose tissue after exposure to cold. Corresponding coronal slices of the MRI-derived fat signal fraction (FSF, %) maps (*D* and *H*) show clavicular depots with a FSF in the range of 50–70% (white ovals). The anatomic location corresponds to the clavicular regions with high SUV on the cold PET scan, and the FSF range agrees with previously published values of BAT (30, 31). Unlike in the PET scan, this region of tissue is visible on MRI regardless of temperature.
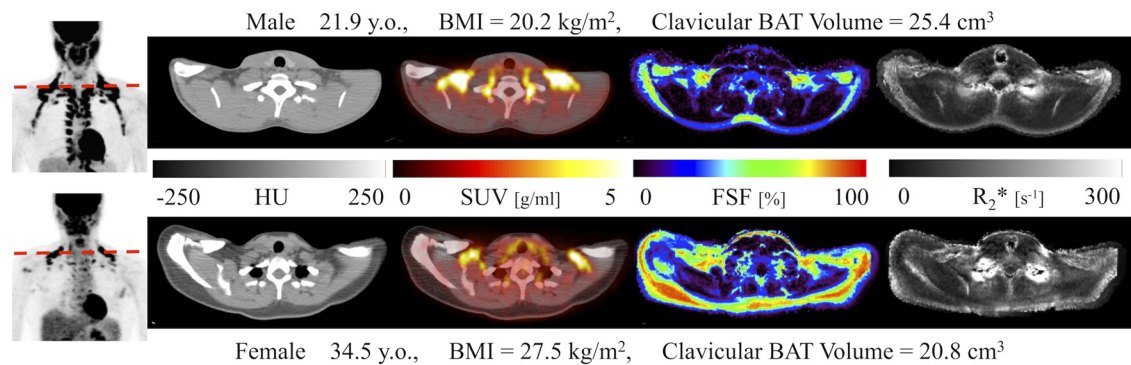
Fig. 4. Clavicular level axial slices from the cold scan of the subjects in Figs. 2 (*top*) and 3 (*bottom*). The dashed red line on the PET maximum intensity projection (MIP; *left*) indicates that the location of the axial slices displayed. The following 4 axial images are, in order, CT Hounsfield hnit (HU), PET standardized uptake value (SUV; g/ml) overlaid on the HU image, MRI-derived fat signal fraction (FSF) map (%), and MRI-derived R_2* map (s^{-1}). Note that whereas the region of clavicular adipose tissue is of comparable size on the CT HU image for both the normal-weight (*top*) and overweight (*bottom*) subject (total volume: 25.4 and 20.8 cm^3, respectively), the clavicular adipose tissue in the normal weight subject has a higher SUV (7.1 ± 2.8 g/ml) over the entire region compared with the lower SUV (3.9 ± 1.3 g/ml) in the overweight subject. Additionally, the region of tissue on the MRI FSF image corresponding to the clavicular adipose tissue on the HU image has a slightly lower FSF in the normal-weight compared with the overweight subject (50.1 ± 15.2 vs. 63.3 ± 15.2%, respectively).

values, trending toward the lower values seen in WAT. This trend is consistent for both thermoneutral and cold conditions of the FSF and R_2* values.

The volume of clavicular BAT in the PET-positive subjects ranged from 1.4 to 57.5 cm^3. Figure 7 shows the variation in BAT volume across both age and BMI. There was no difference in BAT volume between normal-weight females (32.3 ± 15.6 cm^3) and normal weight males (21.6 ± 12.5 cm^3) (P = 0.09). Multiple linear regression was performed on BAT volume using BMI, sex, age, and waist circumference as predictors to determine the relationship between BAT volume and these predictors. The results indicate that only BMI and sex are significantly correlated to BAT volume (BMI: P = 0.04, slope = −5.2; sex: P = 0.03, slope = −21.9), but waist circumference and age are not (waist circumference: P = 0.07, slope = 6.0; age: P = 0.57, slope = 0.8). These results indicate that, for example, if all else were held constant, then in males one could expect a 21.9 cm^3 decrease in BAT volume.

DISCUSSION

Our data suggest that MRI FSF can be used to detect brown adipose regardless of activation status. Furthermore, small but significant reductions in the FSF of BAT can be detected following activation. These findings support MRI as a viable option for studying BAT in adult humans. Additionally, this study extends previous MRI research to quantitatively measure differences in FSF and R_2* values in supraclavicular and subcutaneous adipose tissue depots (30, 44). To the best of our knowledge, this work represents the first study to quantify PET-CT and MRI measurements and to utilize a semiautomated algorithm to identify BAT in the same adults after exposure to both thermoneutral and cold temperatures. Our findings support the use of these metrics to characterize and distinguish between BAT and WAT and lay the foundation for future MRI analysis with the hope that someday MRI-based delineation of BAT can stand on its own. For example, future studies can create an MRI profile of BAT by combining the FSF and R_2* values described here with other previously described metrics such as T_1 (longitudinal relaxation) (23), triglyceride saturation (43), and blood perfusion (12).

MRI-based detection and delineation of BAT from WAT is advantageous because, as we show, MRI can detect BAT under thermoneutral conditions, which is not feasible with [^{18}F]FDG PET. MRI-based detection of inactive BAT is possible because the morphological characteristics such as a lower fat fraction and greater mitochondrial content are present even when not active. Our results support this, as both the FSF and R_2* values are statistically different between BAT and WAT even under thermoneutral conditions. Additionally, MRI is capable of distinguishing between active and inactive BAT. For example, an increase in blood flow or the consumption of fatty acids by active BAT may be detected as a decrease in the FSF. This decrease in FSF is seen in our results, where the FSF is on average 2.2% lower after exposure to cold than to warm temperatures, similar to previously published results (44). Although the FSF values presented here are lower than those reported by Lundström et al. (44), this is likely because of the difference in the manner in which the BAT masks or regions of interest (ROIs) were defined. Lundström et al. (44) used manual ROI definitions, whereas this work utilized PET-CT to restrict and define the spatial location of the BAT ROIs on the MRI. Therefore, we believe the ROIs used here are more rigorous and restrictive. It is possible that the ROIs used by Lundström et al. (44) included tissue that was not BAT, resulting in a higher fat fraction. The goal of future work is to achieve full automation of BAT ROI definition. Although the process applied in this work was not entirely automated, the level of automation performed in this research was a substantial improvement over manual ROI delineation.

The decrease in FSF is also reflected as a statistically significant increase in the HU values after exposure to cold, as has been reported previously (3, 28). These FSF and HU results are consistent because as adipose tissue reduces in fat content the HU values become less negative. Additionally, as expected, given that increased SUV is the currently accepted biomedical imaging indicator for activated BAT, the SUV in clavicular BAT is significantly higher after exposure to cold temperatures. Also, although not significantly different, the normal-weight subjects show higher mean SUV than the overweight subjects. This may indicate that the BAT in overweight sub-

CT HU

PET SUV [g/ml]
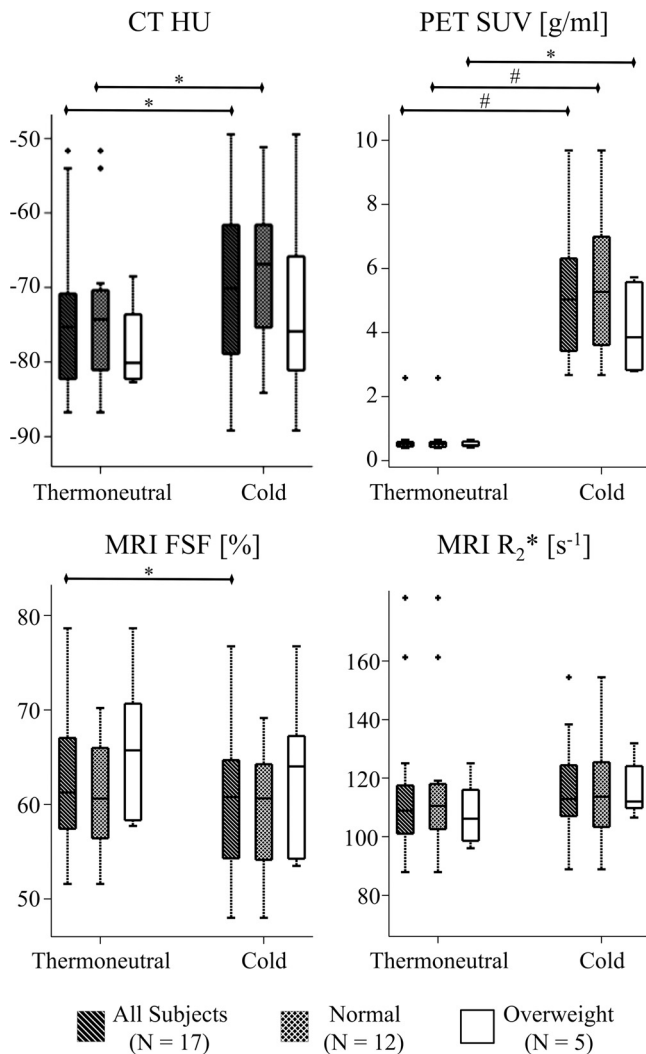
MRI FSF [%]

MRI R$_2$* [s^{-1}]

Fig. 5. Box and whisker plots showing the spread of the CT Hounsfield units (HU), PET standardized uptake value (SUV; g/ml), MRI-derived fat signal fraction (FSF; %), and MRI R$_2$* (s^{-1}) values from both thermoneutral and cold scans of PET-positive subjects. The center line in each box plot indicates the median value, and data values >1.5 times the interquartile range are displayed as individual data points either above or below the box and whisker plot. Statistical comparisons were performed using Wilcoxon signed-rank test: *$P < 0.05$; #$P < 0.01$.

jects is less responsive to cold stimulus or that the overweight subjects did not get cold enough to show increased SUV, as has been shown previously (9, 38, 63).

Although we measured a significant decrease in the FSF values, the difference is slight. Therefore, we note that for future research calculating MRI FSF, it is important to reduce the degree to which other factors may contribute to the change in FSF. This can be accomplished in several ways. First, reducing partial volume effects is beneficial. Partial volume effects occur when the tissue of interest (BAT) is averaged with other tissues due to limited imaging resolution. The clavicular adipose depot is very heterogeneous, containing blood vessels, fascia, and other tissues. This may contribute to partial volume effects, which can be reduced in part with smaller voxels. The BAT mask applied here was eroded at the outer boundary, helping to reduce any partial volume effect at
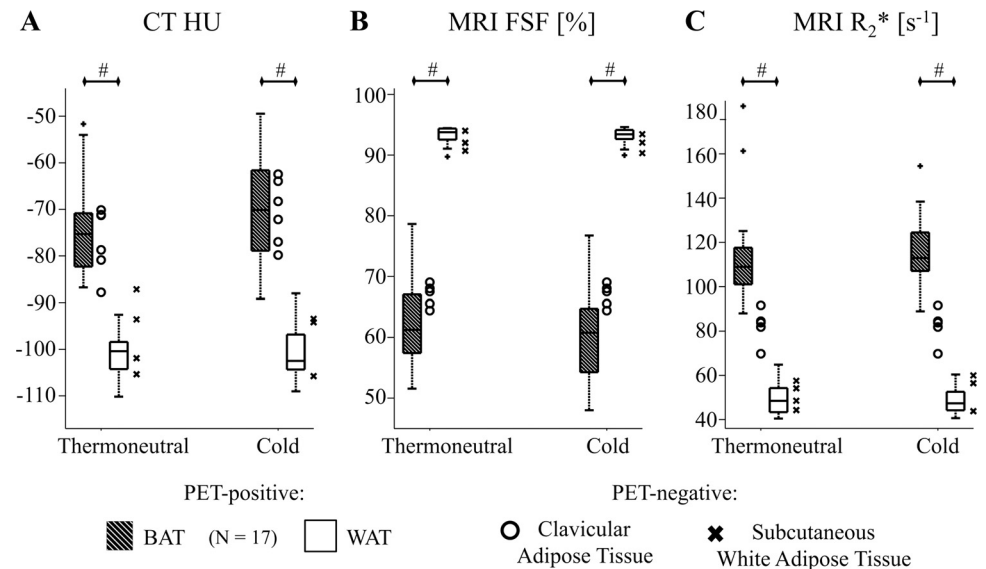
the boundary of the adipose depot. Future work would be improved by obtaining MRI with finer spatial resolution. Second, to obtain a more accurate fat-water separation, the chemical shift of water due to temperature must be taken into account. Because BAT releases heat when activated, this means the tissue becomes warmer than standard body temperature, and the magnetic resonance frequency of water shifts accordingly. The direction of the error in FSF is a function of how fitting the shifted water peak interacts with the acquisition parameters, i.e., the acquired echo times. As Hernando et al. (27) discuss, the temperature-dependent water frequency shift results in a mismatch between the employed signal model and the acquired data. Accounting for temperature-dependent water peak shift is not possible with this data set due to insufficient spectral resolution, i.e., the low number of acquired echoes. However, because this work utilized complex fitting to initialize magnitude fitting, these results should have more moderate temperature-related errors compared with results using only magnitude fitting (27). Third, recent publications indicate the importance of individualized cooling protocols, especially for subjects with higher BMI (37, 57). The goal of the individualized cooling protocol is to replicate the same physiological cold stress across subjects regardless of body type, and although the ambient room temperature and duration of exposure was standardized across subjects in our study, it is likely that many of the normal-weight subjects felt colder than the overweight subjects. Therefore, the BAT in overweight subjects may not have been activated or was not activated for long enough to detect significant lipid oxidation. This is supported in the measurement of the subjects' change in body temperature (ΔT). After 2 h of exposure to cold, the body temperature decreased in normal-weight subjects (-0.19 ± 0.57, $P = 0.03$) but not in overweight subjects (-0.06 ± 0.40, $P = 0.34$). Taking these three factors into account would help ensure that the measured difference between the thermoneutral and cold FSF values is a result of a true metabolic change in the tissue.

One weakness of this study is that it was not designed to compare normal-weight vs. overweight subjects, and as such further research is needed to clarify the relationship between body weight and volume of BAT. Furthermore, although many studies report differences in BAT glucose uptake, to our knowledge this is the first report comparing FSF and HU values of BAT in normal weight with overweight adults. However, because BAT also influences triglyceride metabolism in addition to glucose metabolism, a shortcoming of this study is that the plasma triglyceride levels were not measured. Future studies of human BAT should quantify plasma triglyceride levels.

The results of this research show that the MRI properties of FSF and R$_2$* are capable of distinguishing between clavicular BAT and subcutaneous WAT in adults. Additionally, the separation between the MRI values of BAT and WAT are more clearly distinguishable than the HU values. It is possible that this range of HU values is due to the inhomogeneity of the clavicular adipose tissue, which may contain a range of fatty tissue types, from WAT like in some areas to BAT like in others. The R$_2$* could be detecting blood perfusion in the tissue or iron content due to higher levels of mitochondria, both of which are significantly higher in BAT compared with WAT (14, 51). It is possible that the R$_2$* values reported here are higher compared with previously reported values (30) because

Fig. 6. Comparison of clavicular adipose tissue to umbilicus level subcutaneous white adipose tissue (WAT) in both PET-positive and PET-negative subjects. Data from the clavicular brown adipose tissue (BAT) and subcutaneous WAT of the 17 PET-positive subjects are displayed in box and whisker plots showing the spread of CT Hounsfield units (HU; *A*), MRI-derived fat-signal fraction (FSF; %) (*B*), and MRI R_2^* (s^{-1}; *C*) values from both thermoneutral and cold scans. Data values >1.5 times the interquartile range are displayed as individual data points either above or below the box and whisker plot. Statistical comparison of BAT to WAT for the 17 PET-positive subjects was performed using Wilcoxon rank sum test: #$P < 0.001$. Data from the PET-negative subjects' clavicular adipose tissue (○) and umbilicus level subcutaneous WAT (x) are plotted to the right of each corresponding box and whisker plot.

A CT HU   **B** MRI FSF [%]   **C** MRI R_2^* [s^{-1}]

PET-positive: ◨ BAT (N = 17)   ☐ WAT   PET-negative: ○ Clavicular Adipose Tissue   ✗ Subcutaneous White Adipose Tissue

of the rigorous method of ROI definition used in this work, including WAT-like tissue in the ROI that would cause the R_2^* values to decrease.
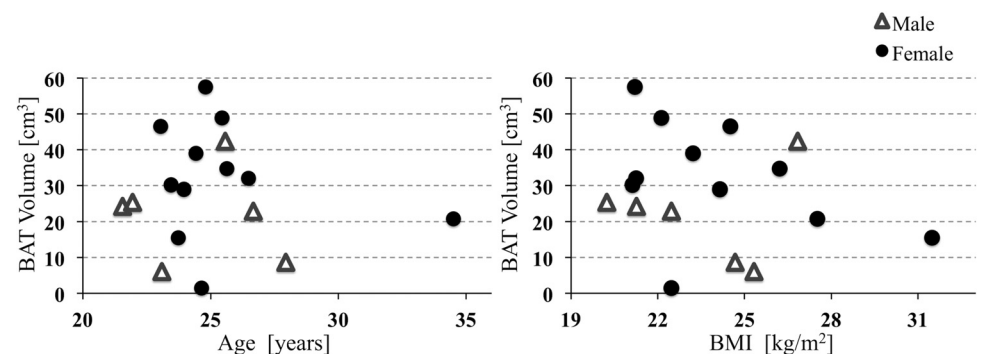
In this research, the prevalence of clavicular BAT as determined using the elevated [^{18}F]FDG levels is 20/24 = 83%. This is derived from the 20 PET activators out of a total of 24 subjects (PET-CT data was not acquired in 1 subject). The range in clavicular BAT volume in these PET-positive subjects is likely indicative of the natural variation of BAT in adult humans. Analyzing the clavicular adipose tissue from the PET-negative subjects shows that the values in their clavicular adipose depots are more similar to the values seen in the PET-positive subjects. Therefore, if we instead use the FSF and R_2^* values to determine the presence of suspected BAT, the prevalence could be closer to 100%. Without biopsy samples of the tissue, it is not possible to determine the true prevalence in this cohort. This illustrates one of the main issues with using PET-CT imaging to detect BAT; it relies on the uptake of [^{18}F]FDG by active brown adipocytes to determine the presence of BAT. Therefore, if no uptake occurs, it is assumed that BAT does not exist in that subject. Previous research shows this is untrue and that brown adipocytes are present in the supraclavicular adipose depot of subjects who are PET negative (42). Biopsy samples of the clavicular adipose depot in these subjects contained mainly unilocular adipocytes, but there existed a scattering of multilocular cells that stained positive for BAT-specific markers such as uncoupling protein 1 (42). Furthermore, other work shows that the supraclavicular adipose tissue of PET-negative subjects is capable of differentiating in vitro into brown adipocytes (41). These two findings demonstrate that the prevalence of BAT in adults may be higher than PET scans indicate, which is exciting when considering the possible role BAT may play in mitigating the metabolic syndromes.

In conclusion, the present study extends the application of MRI to quantifying the MRI FSF and R_2^* properties of BAT in adults. Building on these results with additional MRI-derived properties such as temperature, diffusion, perfusion, and T_1, MRI will be able to distinguish BAT without human subjectivity, even if the tissue is not active. Because some subjects that are PET negative do have BAT, it is important to develop a technique for detecting BAT that does not rely solely on the rate of glucose metabolism. Additionally, the ability to distinguish BAT without ionizing radiation would enable BAT to be studied in larger cohorts, in longitudinal studies, and in difficult populations such as pediatrics, which could further our understanding of the role BAT plays in humans.

In support of reproducible research, figure reproduction scripts and data (17) are freely available for download from a version-controlled source code repository (18) in addition to the specific, tagged release of source code (19) used for this

Fig. 7. Clavicular BAT volume vs. age (*left*) and BMI (*right*) for all 17 PET-positive subjects. Although there is no statistically significant difference between the volume of BAT in males and females, it appears that females tend to have a larger volume of BAT than men, especially when delineated by BMI.

△ Male   ● Female

article. Other related data and code are also publicly accessible (20, 21).

DISCLOSURES

No conflicts of interest, financial or otherwise, are declared by the authors.

AUTHOR CONTRIBUTIONS

A.G., T.F.T., R.C.W., and E.B.W. conception and design of research; A.G. performed experiments; A.G. and E.B.W. analyzed data; A.G., T.F.T., and E.B.W. interpreted results of experiments; A.G. prepared figures; A.G. and E.B.W. drafted manuscript; A.G., T.F.T., R.C.W., M.J.A., and E.B.W. edited and revised manuscript; A.G., T.F.T., R.C.W., M.J.A., and E.B.W. approved final version of manuscript.

REFERENCES

1. **Aschermann Z, Perlaki G, Orsi G, Nagy SA, Horvath A, Bone B, Bihari K, Acs P, Janszky J, Komoly S, Bogner P.** Quantitative assessment of brain iron by R2* relaxometry in patients with cervical dystonia. *Mov Disord* 30: 1422–1426, 2015.
2. **Avram AS, Avram MM, James WD.** Subcutaneous fat in normal and diseased states: 2. Anatomy and physiology of white and brown adipose tissue. *J Am Acad Dermatol* 53: 671–683, 2005.
3. **Baba S, Jacene HA, Engles JM, Honda H, Wahl RL.** CT Hounsfield units of brown adipose tissue increase with activation: preclinical and clinical studies. *J Nucl Med* 51: 246–250, 2010.
4. **Bakker LE, Boon MR, van der Linden RA, Arias-Bouda LP, van Klinken JB, Smit F, Verberne HJ, Jukema JW, Tamsma JT, Havekes LM, van Marken Lichtenbelt WD, Jazet IM, Rensen PC.** Brown adipose tissue volume in healthy lean south Asian adults compared with white Caucasians: a prospective, case-controlled observational study. *Lancet Diabetes Endocrinol* 2: 210–217, 2014.
5. **Bartelt A, Bruns OT, Reimer R, Hohenberg H, Ittrich H, Peldschus K, Kaul MG, Tromsdorf UI, Weller H, Waurisch C, Eychmüller A, Gordts PL, Rinninger F, Bruegelmann K, Freund B, Nielsen P, Merkel M, Heeren J.** Brown adipose tissue activity controls triglyceride clearance. *Nat Med* 17: 200–205, 2011.
6. **Berbée JF, Boon MR, Khedoe PP, Bartelt A, Schlein C, Worthmann A, Kooijman S, Hoeke G, Mol IM, John C, Jung C, Vazirpanah N, Brouwers LP, Gordts PL, Esko JD, Hiemstra PS, Havekes LM, Scheja L, Heeren J, Rensen PCN.** Brown fat activation reduces hypercholesterolaemia and protects from atherosclerosis development. *Nat Commun* 6: 6356, 2015.
7. **Berglund J, Kullberg J.** Three-dimensional water/fat separation and T2* estimation based on whole-image optimization–application in breathhold liver imaging at 1.5 T. *Magn Reson Med* 67: 1684–1693, 2012.
8. **Bligh J, Johnson KG.** Glossary of terms for thermal physiology. *J Appl Physiol* 35: 941–961, 1973.
9. **Blondin DP, Labbé SM, Tingelstad HC, Noll C, Kunach M, Phoenix S, Guérin B, Turcotte ÉE, Carpentier AC, Richard D, Haman F.** Increased brown adipose tissue oxidative capacity in cold-acclimated humans. *J Clin Endocrinol Metab* 99: 438–446, 2014.
10. **Cannon B, Nedergaard J.** Brown adipose tissue: function and physiological significance. *Physiol Rev* 84: 277–359, 2004.
11. **Chen YC, Cypess AM, Chen YC, Palmer M, Kolodny G, Kahn CR, Kwong KK.** Measurement of human brown adipose tissue volume and activity using anatomic MR imaging and functional MR imaging. *J Nucl Med* 54: 1584–1587, 2013.
12. **Chen YI, Cypess AM, Sass a C., Brownell AL, Jokivarsi KT, Kahn CR, Kwong KK.** Anatomical and functional assessment of brown adipose tissue by magnetic resonance imaging. *Obesity (Silver Spring)* 20: 1519–1526, 2012.
13. **Chondronikola M, Volpi E, Borsheim E, Porter C, Annamalai P, Enerback S, Lidell ME, Saraf MK, Labbe SM, Hurren NM, Yfanti C, Chao T, Andersen CR, Cesani F, Hawkins H, Sidossis LS.** Brown Adipose Tissue Improves Whole-Body Glucose Homeostasis and Insulin Sensitivity in Humans. *Diabetes* 63: 4089–4099, 2014.
14. **Cinti S.** The adipose organ. *Prostaglandins Leukot Essent Fatty Acids* 73: 9–15, 2005.
15. **Cypess AM, Chen Y, Sze C, Wang K, English J, Chan O, Holman AR, Tal I, Palmer MR, Kolodny GM, Kahn CR.** Cold but not sympathomimetics activates human brown adipose tissue in vivo. *Proc Natl Acad Sci U S A* 109: 10001–10005, 2012.
16. **Gifford A, Towse TF, Walker RC, Avison MJ, Welch EB.** Human brown adipose tissue depots automatically segmented by positron emission tomography/computed tomography and registered magnetic resonance images. *J Vis Exp*: doi: 10.3791/52415, 2015.
17. **Gifford A, Towse TF, Walker RC, Avison MJ, Welch EB.** *Replication Data for: Characterizing Active and Inactive Brown Adipose Tissue in Adult Humans Using PET-CT and MR Imaging* (Online). Mendeley Data. http://dx.doi.org/10.17632/d4mfxvxjcx.1 [2016].
18. **Gifford A, Towse TF, Walker RC, Avison MJ, Welch EB.** *Replication Code Repository For: Characterizing Active and Inactive Brown Adipose Tissue in Adult Humans Using PET-CT and MR Imaging* (Online). Github. https://github.com/gifforda/AJP_Gifford_MRI_and_PET_CT_Properties_of-_BAT (SHA-1 hash = b13e7213290cc1b57ab4873413d600761d3de8e8) [2016].
19. **Gifford A, Towse TF, Walker RC, Avison MJ, Welch EB.** *Replication code for: Characterizing Active and Inactive Brown Adipose Tissue in Adult Humans Using PET-CT and MR Imaging* (Online). Zenodo. http://dx.doi.org/10.5281/zenodo.50875 [2016].
20. **Gifford A, Walker RC, Towse TF, Welch EB.** *Replication Data for: Correlations Between Quantitative Fat-Water Magnetic Resonance Imaging and Computed Tomography in Human Subcutaneous White Adipose Tissue* (Online). Mendeley Data, v1. http://dx.doi.org/10.17632/pypbrjnp4j.1 [2016].
21. **Gifford A, Walker RC, Towse TF, Welch EB.** *Replication Data for: Correlations Between Quantitative Fat-Water Magnetic Resonance Imaging and Computed Tomography in Human Subcutaneous White Adipose Tissue* (Online). Zenodo. http://dx.doi.org/10.5281/zenodo.34029 [2015].
22. **Gunawardana SC, Piston DW.** Insulin-independent reversal of type 1 diabetes in nonobese diabetic mice with brown adipose tissue transplant. *Am J Physiol Endocrinol Metab* 308: E1043–E1055, 2015.
23. **Hamilton G, Smith DL, Bydder M, Nayak KS, Hu HH.** MR properties of brown and white adipose tissues. *J Magn Reson Imaging* 34: 468–473, 2011.
24. **Heaton JM.** The distribution of brown adipose tissue in the human. *J Anat* 112: 35–39, 1972.
25. **Hernando D, Kramer JH, Reeder SB.** Multipeak fat-corrected complex R2* relaxometry: Theory, optimization, and clinical validation. *Magn Reson Med* 70: 1319–1331, 2013.
26. **Hernando D, Liang ZP, Kellman P.** Chemical shift-based water/fat separation: a comparison of signal models. *Magn Reson Med* 64: 811–822, 2010.
27. **Hernando D, Sharma SD, Kramer H, Reeder SB.** On the confounding effect of temperature on chemical shift-encoded fat quantification. *Magn Reson Med* 72: 464–470, 2014.
28. **Hu HH, Chung a S, Nayak KS, Jackson HA, Gilsanz V.** Differential computed tomographic attenuation of metabolically active and inactive adipose tissues: preliminary findings. *J Comput Assist Tomogr* 35: 65–71, 2011.
29. **Hu HH, Hines CD, Smith DL Jr, Reeder SB.** Variations in T(2)* and fat content of murine brown and white adipose tissues by chemical-shift MRI. *Magn Reson Imaging* 30: 323–329, 2012.
30. **Hu HH, Perkins TG, Chia JM, Gilsanz V.** Characterization of human brown adipose tissue by chemical-shift water-fat MRI. *AJR Am J Roentgenol* 200: 177–183, 2013.

31. **Hu HH, Yin L, Aggabao PC, Perkins TG, Chia JM, Gilsanz V.** Comparison of brown and white adipose tissues in infants and children with chemical-shift-encoded water-fat MRI. *J Magn Reson Imaging* 38: 885–896, 2013.

32. **Hull D.** Heat production in adipose tissue. *Proc R Soc Med* 59: 1278–1280, 1966.

33. **Huttunen P, Hirvonen J, Kinnula V.** The occurrence of brown adipose tissue in outdoor workers. *Eur J Appl Physiol Occup Physiol* 46: 339–345, 1981.

34. **Khalil M, Enzinger C, Langkammer C, Tscherner M, Wallner-Blazek M, Jehna M, Ropele S, Fuchs S, Fazekas F.** Quantitative assessment of brain iron by R(2)* relaxometry in patients with clinically isolated syndrome and relapsing-remitting multiple sclerosis. *Mult Scler* 15: 1048–1054, 2009.

35. **Khedoe PP, Hoeke G, Kooijman S, Dijk W, Buijs JT, Kersten S, Havekes LM, Hiemstra PS, Berbée JF, Boon MR, Rensen PCN.** Brown adipose tissue takes up plasma triglycerides mostly after lipolysis. *J Lipid Res* 56: 51–59, 2015.

36. **Kim S, Lee GH, Lee S, Park SH, Pyo HB, Cho JS.** Body fat measurement in computed tomography image. *Biomed Sci Instrum* 35: 303–308, 1999.

37. **van der Lans AA, Wierts R, Vosselman MJ, Schrauwen P, Brans B, van Marken Lichtenbelt WD.** Cold-activated brown adipose tissue in human adults: methodological issues. *Am J Physiol Regul Integr Comp Physiol* 307: R103–R113, 2014.

38. **van der Lans AA, Hoeks J, Brans B, Vijgen GH, Visser MG, Vosselman MJ, Hansen J, Jörgensen JA, Wu J, Mottaghy FM, Schrauwen P, van Marken Lichtenbelt WD.** Cold acclimation recruits human brown fat and increases nonshivering thermogenesis. *J Clin Invest* 123: 3395–3403, 2013.

39. **Lee P, Linderman JD, Smith S, Brychta RJ, Wang J, Idelson C, Perron RM, Werner CD, Phan GQ, Kammula US, Kebebew E, Pacak K, Chen KY, Celi FS.** Irisin and FGF21 are cold-induced endocrine activators of brown fat function in humans. *Cell Metab* 19: 302–309, 2014.

40. **Lee P, Smith S, Linderman J, Courville AB, Brychta RJ, Dieckmann W, Werner CD, Chen KY, Celi FS.** Temperature-acclimated brown adipose tissue modulates insulin sensitivity in humans. *Diabetes* 177: 1–59, 2014.

41. **Lee P, Swarbrick MM, Zhao JT, Ho KK.** Inducible brown adipogenesis of supraclavicular fat in adult humans. *Endocrinology* 152: 3597–3602, 2011.

42. **Lee P, Zhao JT, Swarbrick MM, Gracie G, Bova R, Greenfield JR, Freund J, Ho KK.** High prevalence of brown adipose tissue in adult humans. *J Clin Endocrinol Metab* 96: 2450–2455, 2011.

43. **Leporq B, Lambert A, Ronot M, Vilgrain V, Van Beers BE.** Quantification of the triglyceride fatty acid composition with 3.0 T MRI. *NMR Biomed* 27: 1211–1221, 2014.

44. **Lundström E, Strand R, Johansson L, Bergsten P, Ahlström H, Kullberg J.** Magnetic resonance imaging cooling-reheating protocol indicates decreased fat fraction via lipid consumption in suspected brown adipose tissue. *PLoS One* 10: e0126705, 2015.

45. **Maes F, Collignon a Vandermeulen D, Marchal G, Suetens P.** Multimodality image registration by maximization of mutual information. *IEEE Trans Med Imaging* 16: 187–198, 1997.

47. **Middleton MS, Hamilton G, Bydder M, Sirlin CB.** How Much Fat is Under the Water Peak in Liver Fat MR Spectroscopy? In: *17th annual meeting of ISMRM*, Honolulu, HI, 2009, p. 4331.

48. **Norheim F, Langleite TM, Hjorth M, Holen T, Kielland A, Stadheim HK, Gulseth HL, Birkeland KI, Jensen J, Drevon a C.** The effects of acute and chronic exercise on PGC-1α, irisin and browning of subcutaneous adipose tissue in humans. *FEBS J* 281: 739–749, 2014.

49. **Ouellet V, Labbé SM, Blondin DP, Phoenix S, Guérin B, Haman F, Turcotte EE, Richard D, Carpentier AC.** Brown adipose tissue oxidative metabolism contributes to energy expenditure during acute cold exposure in humans. *J Clin Invest* 122: 545–552, 2012.

50. **Ouellet V, Routhier-Labadie A, Bellemare W, Lakhal-Chaieb L, Turcotte E, Carpentier AC, Richard D.** Outdoor temperature, age, sex, body mass index, and diabetic status determine the prevalence, mass, and glucose-uptake activity of 18F-FDG-detected BAT in humans. *J Clin Endocrinol Metab* 96: 192–1299, 2011.

51. **Porter C, Malagaris I, Sidossis LS.** Is the heat surrounding adipose tissue mitochondria warranted? *Curr Opin Clin Nutr Metab Care* 17: 503–508, 2014.

52. **Rasmussen JM, Entringer S, Nguyen A, Van Erp TGM, Guijarro A, Oveisi F, Swanson JM, Piomelli D, Wadhwa PD, Buss C, Potkin SG.** Brown adipose tissue quantification in human neonates using water-fat separated MRI. *PLoS One* 8: e7790, 2013.

54. **Saito M, Okamatsu-Ogura Y, Matsushita M, Watanabe K, Yoneshiro T, Nio-Kobayashi J, Iwanaga T, Miyagawa M, Kameya T, Nakada K, Kawai Y, Tsujisaki M.** High incidence of metabolically active brown adipose tissue in healthy adult humans: effects of cold exposure and adiposity. *Diabetes* 58: 1526–1531, 2009.

55. **Smith RE, Horwitz BA.** Brown fat and thermogenesis. *Physiol Rev* 49: 330–425, 1969.

56. **Tsao J, Samsonov A, Hu HH, Hurley S, Jiang Y, Hernando D, Reeder S, Sirlin C.** 2012 ISMRM challenge on water-fat reconstruction judging [Online]. *Int Soc Magn Reson Med* 2012. http://www.webcitation.org/6bxPUKgNR [1 Oct 2015].

56a. **van Marken Lichtenbelt WD, Vanhommerig JW, Smulders NM, Drossaerts JM, Kemerink GJ, Bouvy ND, Schrauwen P, Teule GJ.** Cold-activated brown adipose tissue in healthy men. *N Engl J Med* 360: 1500–1508, 2009.

56b. **van Rooijen BD, van der Lans AA, Brans B, Wildberger JE, Mottaghy FM, Schrauwen P, Backes WH, van Marken Lichtenbelt WD.** Imaging cold-activated brown adipose tissue using dynamic T2*-weighted magnetic resonance imaging and 2-deoxy-2-[18F]fluoro-D-glucose positron emission tomography. *Invest Radiol* 48: 708–714, 2013.

57. **Vijgen GH, Bouvy ND, Teule GJJ, Brans B, Schrauwen P, van Marken Lichtenbelt WD.** Brown adipose tissue in morbidly obese subjects. *PLoS One* 6: e17247, 2011.

58. **Virtanen KA, Lidell ME, Orava J, Heglind M, Westergren R, Niemi T, Taittonen M, Laine J, Savisto N, Enerbäck S, Nuutila P.** Functional brown adipose tissue in healthy adults. *N Engl J Med* 360: 1518–1525, 2009.

59. **Vosselman MJ, Van Der Lans AA, Brans B, Wierts R, Van Baak MA, Schrauwen P, Van Marken Lichtenbelt WD.** Systemic β-adrenergic stimulation of thermogenesis is not accompanied by brown adipose tissue activity in humans. *Diabetes* 61: 3106–3113, 2012.

60. **Wang GX, Zhao XY, Meng ZX, Kern M, Dietrich A, Chen Z, Cozacov Z, Zhou D, Okunade AL, Su X, Li S, Blüher M, Lin JD.** The brown fat-enriched secreted factor Nrg4 preserves metabolic homeostasis through attenuation of hepatic lipogenesis. *Nat Med* 20: 1436–1443, 2014.

61. **Welch EB, Smith DS, Avison MJ, Berglund J, Kullberg J, Ahlström H.** 2012 ISMRM challenge on water-fat reconstruction final team standings (Online). *Int Soc Magn Reson Med* 2012. http://www.webcitation.org/6bxOBP0Ql [1 Oct 2015].

62. **Wood JC, Enriquez C, Ghugre N, Tyzka JM, Carson S, Nelson MD, Coates TD.** MRI R2 and R2* mapping accurately estimates hepatic iron concentration in transfusion-dependent thalassemia and sickle cell disease patients. *Blood* 106: 1460–1465, 2005.

63. **Yoneshiro T, Aita S, Matsushita M, Kayahara T, Kameya T, Kawai Y, Iwanaga T, Saito M.** Recruited brown adipose tissue as an antiobesity agent in humans. *J Clin Invest* 123: 3404–3408, 2013.

64. **Yoshizumi T, Nakamura T, Yamane M, Islam AH, Menju M, Yamasaki K, Arai T, Kotani K, Funahashi T, Yamashita S, Matsuzawa Y.** Abdominal fat: standardized technique for measurement at CT. *Radiology* 211: 283–286, 1999.

65. **Yu H, Shimakawa A, Hines CD, McKenzie CA, Hamilton G, Sirlin CB, Brittain JH, Reeder SB.** Combination of complex-based and magnitude-based multiecho water-fat separation for accurate quantification of fat-fraction. *Magn Reson Med* 66: 199–206, 2011.